Journal of Structural Geology 32 (2010) 478–489

Contents lists available at ScienceDirect

Journal of Structural Geology

journal homepage: www.elsevier.com/locate/jsg

Preferred orientation of phyllosilicates: Comparison of fault gouge, shale and schist

Hans-Rudolf Wenk*, Waruntorn Kanitpanyacharoen, Marco Voltolini

Department of Earth and Planetary Science, University of California, Berkeley, CA 94720, USA

ARTICLE INFO

Article history:
Received 22 March 2009
Received in revised form
6 January 2010
Accepted 17 February 2010
Available online 1 March 2010

Keywords:
Phyllosilicate fabrics
Fault gouge
Shale
Schist

ABSTRACT

Samples of fault gouge from the San Andreas Fault drill hole (SAFOD), a shale from the North Sea sedimentary basin and schists from metamorphic rocks in the Alps have been analyzed with high energy synchrotron X-rays to determine preferred orientation of mica and clay minerals. The method relies on obtaining 2D diffraction images which are then processed with the crystallographic Rietveld method, implemented in the software MAUD, allowing for deconvolution of phases and extraction of their orientation distributions. It is possible to distinguish between detrital illite/muscovite and authigenic illite/smectite, kaolinite and chlorite, and muscovite and biotite, with strongly overlapping peaks in the diffraction pattern. The results demonstrate that phyllosilicates show large texture variations in various environments, where different mechanisms produce the rock microfabrics: fault gouge fabrics are quite weak and asymmetric with maxima for (001) in the range of 1.5–2.5 multiples of random distribution (m.r.d.). This is attributed to heterogeneous deformation with randomization, as well as dissolution–precipitation reactions. Shale fabrics have maxima ranging from 3 to 9 m.r.d. and this is due to sedimentation and compaction. The strongest fabrics were observed in metamorphic schists (10–14 m.r.d.) and developed by deformation as well as recrystallization in a stress field. In the analyzed samples, fabrics of co-existing quartz are weak. All phyllosilicate textures can be explained by orientation of (001) platelets, with no additional constraints on *a*-axes.

1. Introduction

Phyllosilicates in many rocks are distinctly oriented. In fact, their alignment often defines the macroscopic schistosity, bedding plane, and cleavage. Phyllosilicates differ from many other rock-forming minerals by their dominant platy morphology with (001) as both sheet and cleavage plane. Also, anisotropy of physical properties is extreme, with elastic stiffness more than three times higher parallel to the sheet plane than perpendicular to it. Grain shape and physical properties play a major role in the alignment of these minerals, e.g., during compaction of a sediment, ductile deformation or crystallization under stress. Much early work has been dedicated to quantify the alignment of mica platelets which can be easily measured with the universal stage and petrographic microscope (e.g., Sander, 1930). Interestingly, already Sander (1934) used X-ray diffraction to characterize preferred orientation in shale (e.g., his Figure 14). With advances in X-ray diffraction techniques, a pole figure goniometer method in transmission geometry was applied to fine-grained slates (e.g., Oertel, 1983) and this method was refined by Van der Pluijm et al., 1994. The method relies on positioning the detector at the Bragg angle for a basal reflection diffraction peak and recording intensity changes with sample orientation.

Thus, a fair amount of information is available about (001) phyllosilicate pole figures in a variety of rocks, including gneisses, schists, slates and, more recently, shales. The investigations document considerable diversity that depends on formation conditions and compositions.

With the universal stage and with X-ray pole figure goniometry only (001) pole figures can be measured, and thus, there is currently very little information about the orientation of *a*-axes. Furthermore, gouge, shales and schists are composed of many phases with strongly overlapping diffraction peaks. This applies particularly to the 10 Å peak that is used for most pole figure goniometry measurements. In shales, the detrital illite/muscovite peak is overlapped with the authigenic illite/smectite peak; in schists, the muscovite peak is superposed on the biotite peak, and these distinct phases cannot be separated. Here a diffraction method that relies on full diffraction spectra, rather than individual diffraction peaks has advantages (e.g., Lonardelli et al., 2005) and we apply it in this study to quantify preferred orientation of major mineral components of three samples from the drill core of the

* Corresponding author.
E-mail address: wenk@berkeley.edu (H.-R. Wenk).

0191-8141/$ – see front matter © 2010 Elsevier Ltd. All rights reserved.
doi:10.1016/j.jsg.2010.02.003

Table 1
Details about sample locations.

SAFOD #1 arkose Box 20, Run 4 (18–20 cm) 3064.5 m, 5025_1_C_4
SAFOD #2 gouge Box 23, Run 5 (14–18 cm) 3067.0 5025_1_C_5
SAFOD #3 sheared sandstone-gouge Hole G, Run 2, Section 4, 3149 m
Kimmeridge shale, North Sea drill hole, 3750 m
Brg 929, Folded graphite schist, Septimer Pass, Cureglia, 2500 m
Brg 1118 Phyllite, folded, Vor dem Berg, Val Bergalga (Avers), 2680 m
Brg 1295 Schist, Plan Väst above Soglio, Bergell Alps, 1850 m

SAFOD project in the vicinity of the San Andreas fault, a shale, and three metamorphic schists.

2. Samples, experimental techniques and data analysis

Location information of the samples is summarized in Table 1. The San Andreas Fault Observatory at Depth (SAFOD) is a project to investigate mechanical, seismic and chemical processes in situ at depth, as well as providing samples for detailed laboratory analysis (Hickman et al., 2004). We analyzed three samples of clay-rich arkosic composition from shear zones that are, however, not the main San Andreas fault zone. In the following discussion we refer to the samples as SAFOD #1 (Box 20, Run 4 (18–20 cm) 3064.5 m, 5025_1_C_4), SAFOD #2 (Box 23, Run 5 (14–18 cm) 3067.0 m, 5025_1_C_5) and SAFOD #3 (Hole G, Run 2, section 4, 3149 m) (see also: http://www.icdp-online.org/contenido/icdp/front_content.php?idart=1037). Similar samples were analyzed for mineralogical composition and microstructure and we will not go into those details (Schleicher et al., 2006; Solum et al., 2006). There is considerable heterogeneity, particularly in SAFOD #2 and #3 with local shear bands. SEM micrographs reveal a complex microstructure with detrital quartz, feldspars, mica and authigenic illite/smectite clay (Fig. 1a–d). SAFOD #3 displays a very fine-grained matrix with folded veins of calcite (Fig. 1c).

The shale of Kimmeridge age is from a borehole in the North Sea at 3750 m depth (Hornby, 1998). It has a porosity of 2.5% and, based on infrared spectrometry, a composition of 35% illite/smectite/mica, 22% kaolinite, 30% quartz, 5% albite and 4% pyrite was suggested (new results, discussed below, suggest a somewhat different composition). The shale has a high elastic anisotropy as determined from ultrasound velocity measurements ($C_{11} = 49.8$ GPa, $C_{33} = 29.5$ GPa, where C_{33} is perpendicular to the bedding plane). The microstructure reveals clearly detrital micaceous particles, as well as authigenic clay (Fig. 1d).

Three schists are from greenschist facies rocks of the upper Pennine Suretta nappe in the central Alps in Grisons, Switzerland. Brg 929 is a phyllite from Cureglia (2500 m), near Septimer Pass. The sample contains muscovite with subordinate chlorite. There is a fine-grained population and coarser crystals. The larger crystals are mechanically bent, and occasionally kinked, in fold-like structures (Fig. 2a). Brg 1118 is a fine-grained muscovite-graphite schist with albite porphyroclasts from Vor dem Berg (2680 m) in Val Bergalga (Avers). Fine-grained muscovite is concentrated in layers and highly aligned. Some clusters of larger muscovite crystals (up to 0.5 mm) are more randomly oriented (Fig. 2b). Brg 1295 is a fine-grained biotite–muscovite schist from the base of the Suretta nappe near Plan Väst, 1850 m and is of higher metamorphic grade. Biotite is strongly aligned, muscovite and chlorite are generally fine-grained and associated with alteration of feldspars (Fig. 2c).

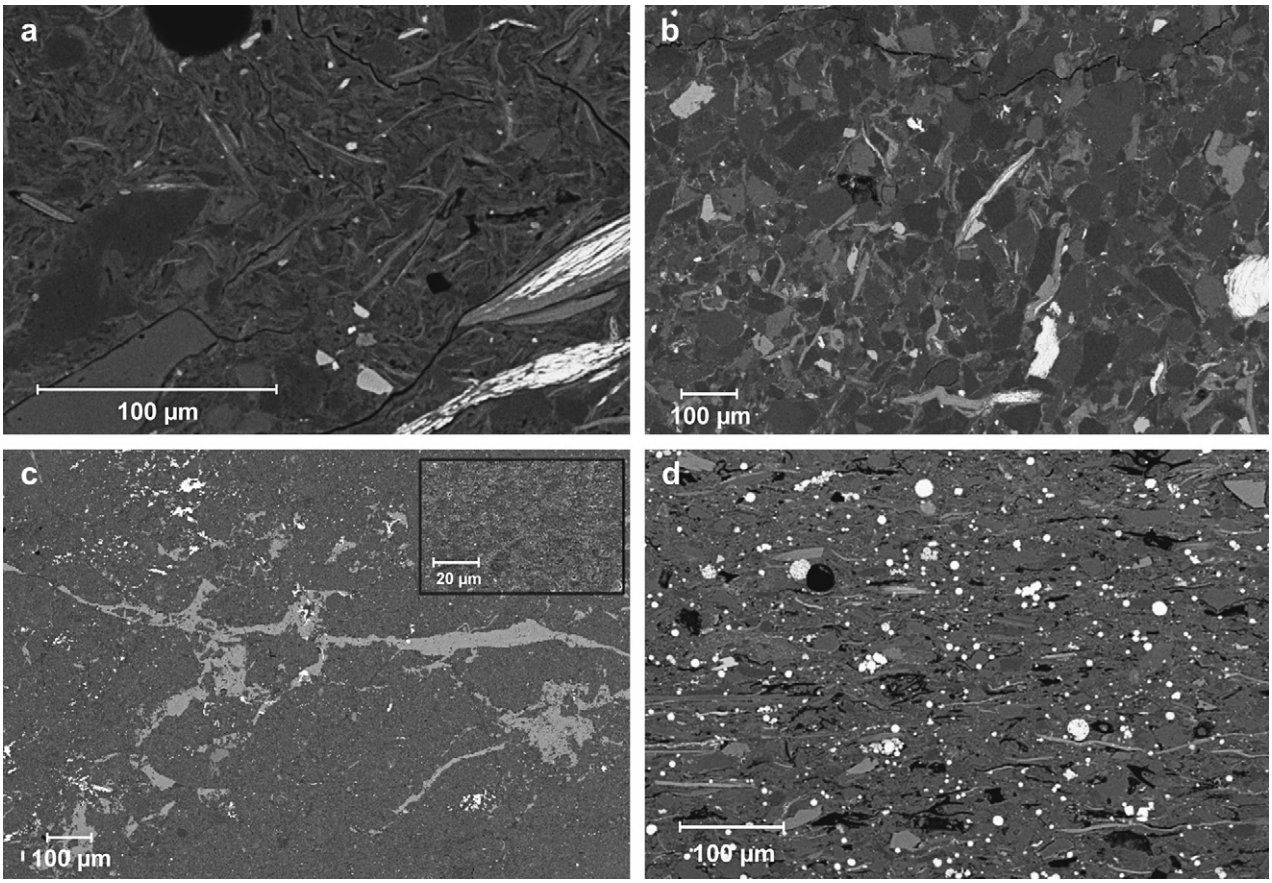

Fig. 1. Backscattered SEM images of samples from SAFOD and Kimmeridge shale (Hornby, 1998). (a) and (b) SAFOD #2, (c) SAFOD #3, and (d) shale. Bright particles are rich in heavy elements such as pyrite spherulites in shale (d). Dark zones indicate porosity.

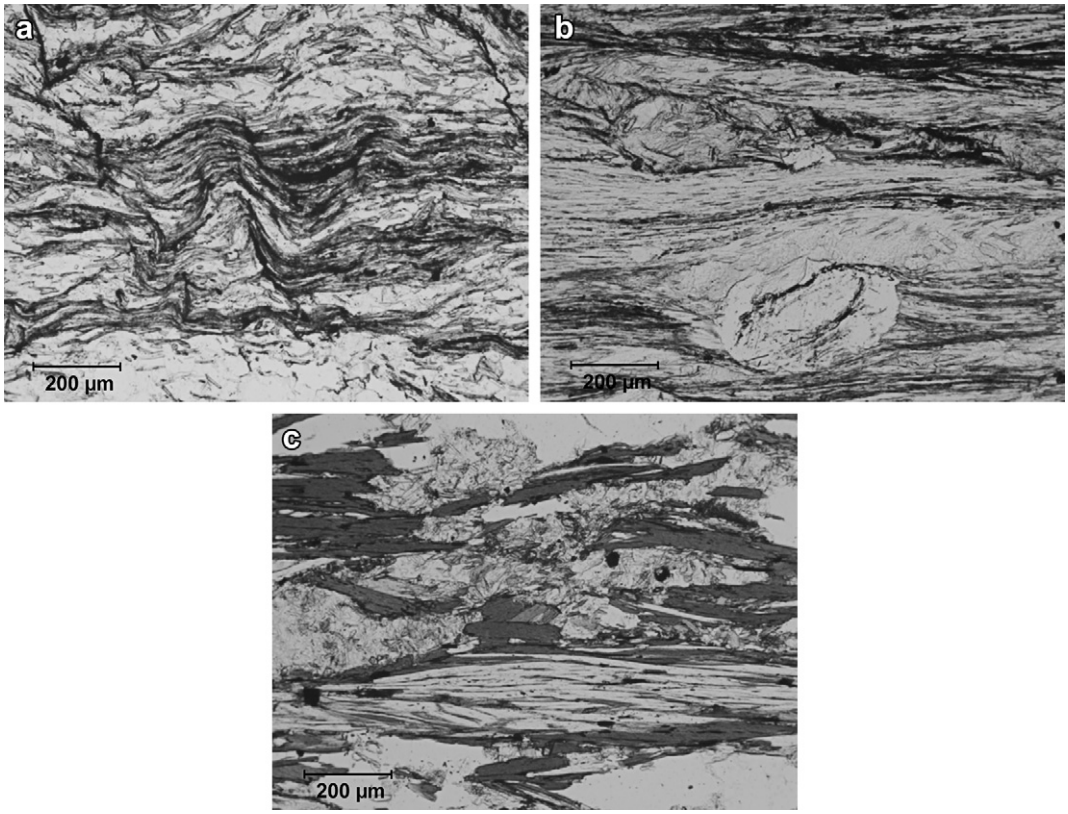

Fig. 2. Optical micrographs of greenschist facies schists. Plane polars. (a) Brg 929 muscovite–chlorite schist with local crenulation folds. (b) Brg 1118 graphite-bearing muscovite–chlorite phyllite with albite porphyroclast. (c) Brg 1295 biotite–muscovite chlorite schist. Note the two generations of muscovite, one interlayered with biotite and the second as alteration of feldspar.

Samples were first embedded in epoxy. Then 2 mm-thick slices were prepared with a microsaw, using kerosene as a cooling agent. The surface of the slice was about 1 cm^2. These slices were then used for synchrotron diffraction experiments in transmission. The method has been described by Wenk et al. (2008a) in some detail.

The samples were measured at the high-energy beamline BESSRC 11-ID-C of APS (Advanced Photon Source) of Argonne National Laboratory, with a monochromatic wavelength of 0.107863 Å. At these short wavelengths X-rays can penetrate mm of material without significant absorption and thus can be used to analyze large volumes, comparable to neutrons. Contrary to neutrons, X-ray data collection can be done much faster (100 s versus hours). Beam-size was 0.5 × 0.5 mm and sample to detector distance was about 2 m. The sample slabs were mounted on a metal rod approximately perpendicular to the bedding/schistosity plane and parallel to the horizontal axis of a goniometer. Images were recorded with a Mar345 image plate detector (3450 × 3450 pixels). Shale and schist samples were translated during data collection, parallel to the horizontal axis, over 5 spots in 2 mm increment to obtain a representative average. For fault gouge, because of the high heterogeneity, local textures were determined.

Three diffraction images are shown in Fig. 3. Intensity variations along the Debye rings immediately reveal preferred orientation. Looking at the 10 Å illite/mica peak, it is obvious that preferred orientation is strongest in schist, intermediate in shale and weak in fault gouge.

Images were recorded at 11 different ω tilt angles, tilting the samples around the horizontal axis in 10° increments (−50°, −40°,

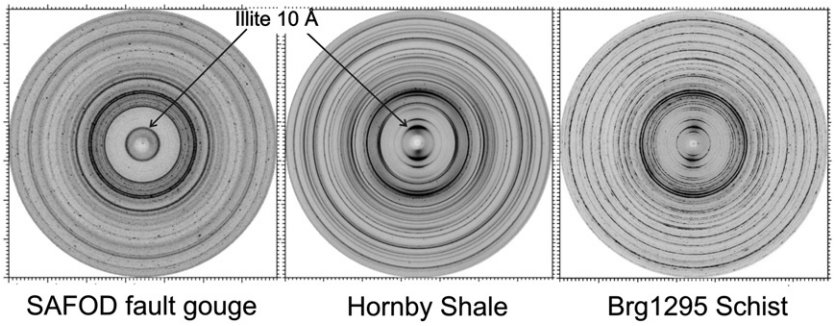

Fig. 3. Diffraction images of SAFOD #1 fault gouge (illite/smectite and illite/mica), Kimmeridge shale (chlorite, illite/smectite, illite/muscovite, kaolinite) and Brg 1295 metamorphic schist (biotite, muscovite, chlorite). Intensity variations along Debye rings are indicative of texture. It is particularly evident for the inner rings (high *d*-spacings). Arrow points to 10 Å diffraction from (002) illite.

−30°, −20°, −10°, 0°, 10°, 20°, 30°, 40°, 50°). In the 0° tilt position, the sample slab is perpendicular to the beam. Combining images at different tilt angles provides larger pole figure coverage for texture analysis. We have tried different coverage strategies and there are minor influences on results, particularly the shape of the (001) texture maximum. Initially we rotated around the normal to the foliation, then chose a direction in the foliation plane. More recently we prefer a somewhat oblique direction. In the case of the fairly coarse-grained schists, two sections, cut at right angles and both perpendicular to the foliation, were combined. At the end of the analysis, orientation distributions for shale and schists were rotated to conform with macroscopic bedding plane and schistosity plane, respectively. For fault gouge, with locally heterogeneous textures, orientations are arbitrary.

After data collection, images were further processed in Fit2D (Hammersley, 1998), following the procedure described at http://eps.berkeley.edu/~wenk/TexturePage/MAUD.htm. First, a CeO_2 powder standard was used to calibrate the sample to detector distance and detector orientation. For each shale image, the image center was refined. The image was then divided into 10° azimuthal sectors and integrated over each sector to obtain spectra, resulting in 36 spectra for each 2D image and $11 \times 36 = 396$ for each sample (esg files). These spectra, each representing differently oriented lattice planes, were later exported from Fit2D and used in the Rietveld refinement. For the Rietveld refinement, we applied the program MAUD (Material Analysis Using Diffraction), which is a code written in Java (Lutterotti et al., 1997). MAUD is unique among Rietveld codes in that it provides sophisticated methods for quantitative texture analysis. The *d*-range used for the analysis is from 1.2 Å to 15 Å. Extending the *d*-range to lower *d*-spacings did not improve results. Fig. 4 shows some spectra of SAFOD #3, shale and schist Brg 1295. The scale is $Q\,(2\pi/d)$ to avoid compression of the spectrum towards low *d*-spacings. The peak profiles illustrate the complexity, with many overlapping peaks.

The Rietveld analysis needs, as input, crystal structures for the mineral phases that are present. For the phyllosilicates, we used for monoclinic illite/muscovite Gualtieri (2000), based on Collins and Catlow (1992), for illite/smectite Plançon et al. (1985), for triclinic kaolinite Bish (1993), based on Bish and Von Dreele (1989), for montmorillonite Tsipursky and Drits (1984) (see also Lutterotti et al., 2010), for triclinic chlorite penninite refined by Joswig et al. (1980), for monoclinic chlorite clinochlore of Rule and Bailey (1987), for monoclinic 2 M muscovite Guggenheim et al. (1987), for monoclinic 2 M biotite Redhammer and Roth (2002), and for triclinic analcite Knowles et al. (1965). The structural data were imported as "crystallographic information files" (cif) from American Mineralogist Crystal Structure Data Base (Downs and Hall-Wallace, 2003). In fault gouge, as well as shale, the illite (002) peak at 10.0 Å ($Q = 0.63$ Å^{-1}) has an asymmetric extension towards higher *d*-spacings (lower *Q*) and this is due to a combination of detrital illite/muscovite and illite/smectite with interlayers and stacking disorder (Fig. 4a, b). For conventions about monoclinic crystal symmetry, see Matthies and Wenk (2009).

First, instrumental parameters such as the center of the ring, the background parameters (three for each spectrum), and the scale parameters (one for each image) were refined. The scale parameters take into account different absorptions and effective sample volumes with tilt, as well as fluctuations in beam intensity. The second step is to extract weight fractions for each phase (quantitative phase analysis) and refine structural and microstructural parameters, including lattice parameters and anisotropic crystallite size (Popa, 1998). Atomic coordinates, site occupancies and temperature factors were held constant because of the high number of variables and the low symmetry of phases. However, sheet silicate composition was refined, especially adding iron to illite, which greatly improved the fit. In the last step, a modified EWIMV algorithm related to WIMV (Matthies and Vinel, 1982) was used for texture analysis. The continuous 3-dimensional orientation distribution function (ODF) is divided into a discrete cell structure with an angular resolution of 10°. Textures were refined for major phases illite/mica, illite/smectite, montmorillonite, chlorite, kaolinite, muscovite, biotite, graphite and quartz.

Fig. 5 shows 2D map plots of some of the samples for the 0° tilt angle image. They represent stacks of the 36 diffraction images. The Rietveld refinements are at the top while observations are at the bottom. The comparison is excellent, both in peak positions and intensity variations, and indicates that the refinement is reliable.

Orientation distributions for all phases were exported from MAUD and further processed in BEARTEX (Wenk et al., 1998). We note that the second crystallographic is used for monoclinic crystals, with the *y*-axis as the unique axis and (010) as mirror plane, whereas MAUD and BEARTEX use the first setting with the *z*-axis as the unique axis. This is a standard in physics and facilitates calculation of physical properties. To convert from one setting to the other, proper transformations need to be done (Matthies and Wenk, 2009). While all calculations are done in first setting, labels on pole figures and diffraction patterns refer to the more commonly used second setting (with (001) corresponding to the phyllosilicate cleavage plane). In BEARTEX, the ODF was smoothed with a 7.5° filter to alleviate artifacts from the ODF cell structure. Pole densities are normalized so that the integral over a pole figure is 1.0 and densities are expressed in multiples of a random distribution (m.r.d.). We show (001) and (100) pole figures for sheet silicates and quartz.

3. Results

All samples have quite complex mineralogical compositions. Phase proportions (in weight fractions) obtained with the Rietveld refinement are summarized in Tables 2. For samples that were analyzed with other methods there is fair agreement, keeping in mind that these were not identical specimens and there is considerable heterogeneity. Particularly for Kimmeridge shale our analysis suggests more 2:1 and less 1:1 phyllosilicates, and less quartz than Hornby (1998). It is conceivable that in this shale some silica is amorphous and is not included in our diffraction analysis. Kimmeridge shale and Brg 1118 schist are mainly composed of phyllosilicates. In all others, quartz and feldspars dominate. Other phases are calcite, analcite, pyrite and graphite.

Textures for SAFOD samples are weak and asymmetric (Fig. 6). Texture strength is higher for detrital illite than for illite/smectite, but the patterns are similar. This can also be verified on the map plot (Fig. 5a). The asymmetry is due to the fact that in all samples there was no obvious macroscopic foliation. The sample was also quite heterogeneous and we picked local fracture zones to perform the texture analysis. Fig. 7 shows diffraction images at various spots. The strongest texture was observed in SAFOD #1 arkose (Fig. 7a). Especially for sample SAFOD #3 (Fig. 7c, d), with a very weak texture, most regions were completely random (Fig. 7d). The insert in Fig. 4a shows details of the 10 Å peak. It is composed of a sharper component at higher *Q*, due to illite/mica and a broader, more diffuse peak at lower *Q* attributed to illite/smectite.

Kimmeridge shale is very rich in phyllosilicates, mainly illite/smectite and illite/muscovite. But there is a significant amount of kaolinite (at $d = 7$ Å, $Q = 0.9$ Å^{-1}) and montmorillonite (small and broad peak at $d = 14$ Å, $Q = 0.45$ Å^{-1}). All sheet silicates have a (001) maximum perpendicular to the bedding plane (Fig. 8). It is strongest for kaolinite (5.6 m.r.d.) and weakest for montmorillonite (1.7 m.r.d.). Similar to SAFOD #1 and #2, there is a bimodal peak at $d = 10$ Å ($Q = 0.63$ Å^{-1}), representing detrital illite at higher *Q*, and authigenic illite/smectite at lower *Q* (see insert in Fig. 5b).

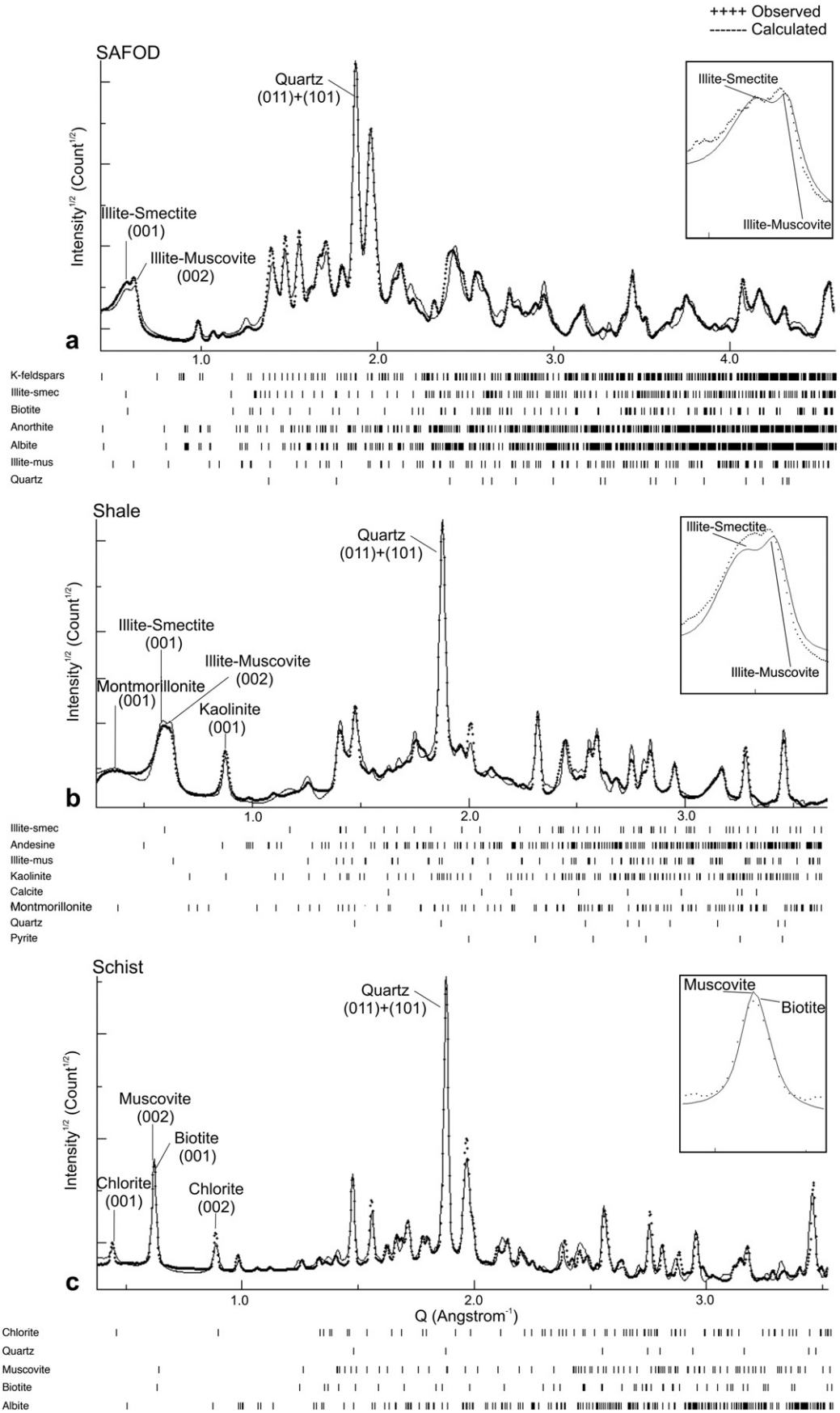

Fig. 4. Diffraction patterns of (a) SAFOD #1 fault gouge, (b) Kimmeridge shale and (c) Brg 1295 metamorphic schist. Scale is $Q\,(2\pi/d)$. Inserted on the right side is an enlargement of the $d = 10$ Å peak which is a superposition of detrital illite/mica and authigenic illite/smectite (a, b) and muscovite and biotite (c). Dots are measurements and solid line the Rietveld fit. Below each spectrum are diffraction peaks of contributing mineral phases.

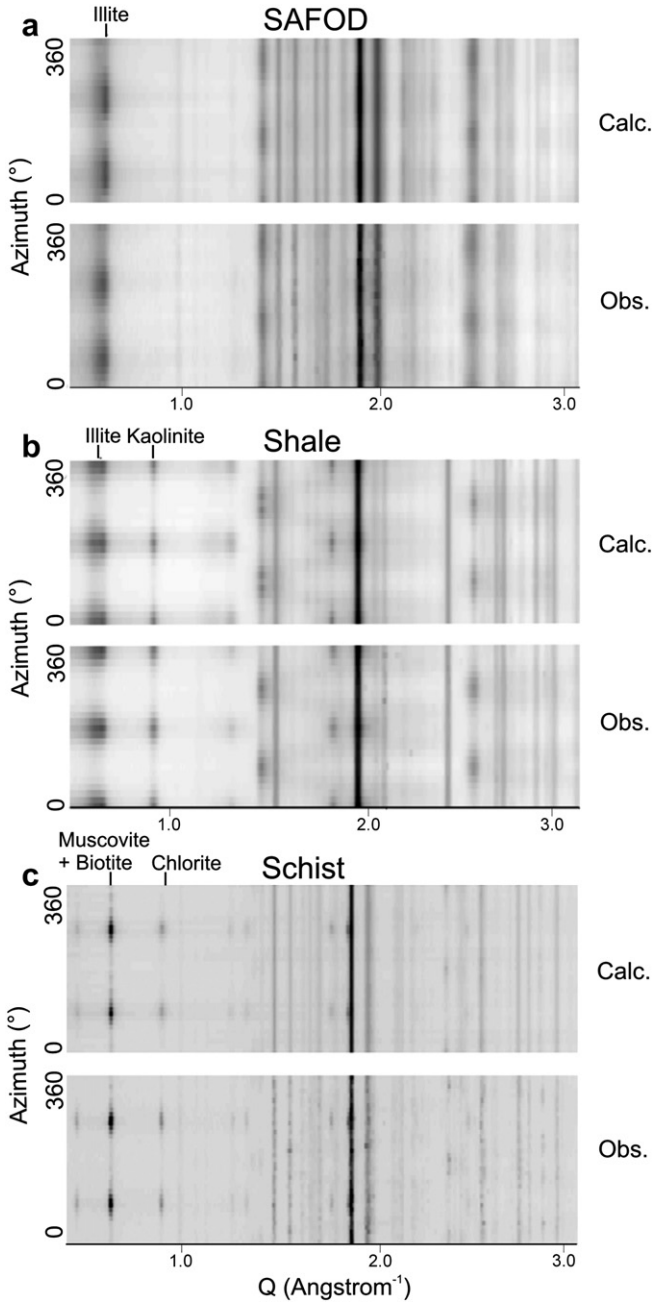

Fig. 5. Two-dimensional map plots comparing observed (bottom) and calculated spectra (top) for image taken at 0° tilt. The image represents stacks of 36 diffraction spectra averaged over 10° azimuthal intervals. Diffraction patterns of (a) SAFOD #1 fault gouge, (b) Kimmeridge shale and (c) Brg 1295 metamorphic schist. Scale is $Q\,(2\pi/d)$.

Significantly, quartz displays weak preferred orientation with *c*-axes aligned in the bedding plane (1.1 m.r.d.). For fault gouge and shale, phyllosilicate (100) pole figures display a uniform girdle around the (001) texture maximum (not shown).

Schists have the strongest textures with 13.5 m.r.d. for (001) of chlorite in Brg 929 and 10.1 m.r.d. for (001) of biotite in Brg 1295 (Fig. 9). Also, in schists, there are significant peak overlaps, especially biotite and muscovite (in Brg 1295), and graphite and quartz (in Brg 1118) but the refinement succeeds in separating them. In schists Brg 929 and Brg 1118, there is a slight alignment of *a*-axes of muscovite and chlorite (Fig. 10). Contrary to shale, the (001) texture maximum is not quite circular, spreading on a great circle perpendicular to the lineation. While micas are strongly aligned, preferred orientation of quartz is almost random (not shown).

Table 2
Phase proportions (in weight %) for samples analyzed in this study.

	SA #1	SA #2	SA#3	Hornby	Brg 929	Brg 1118	Brg 1295
Illite/mica	29.9	45.2	14.1	28.7			
Biotite							6.0
Muscovite					27.4	52.9	10.3
Illite/smectite	6.9	27.3	20.2	43.2			
Montmorillonite				0.9			
Chlorite					16.1	16.9	7.9
Kaolinite				4.8			
Graphite						0.1	
Analcite			4.2				
Quartz	18.9	12.4	43.6	14.8	44.8	30.0	42.7
Plagioclase	44.3	15.1	17.9	2.7	11.7		33.1
Pyrite				4.8			
Calcite				0.1			

4. Discussion

In this study of phyllosilicate textures in seven different rock samples with synchrotron X-ray diffraction, we succeeded for the first time in resolving quantitatively overlapping peaks such as detrital illite/muscovite and authigenic illite/smectite (~10Å), kaolinite and chlorite (~7 Å), and muscovite and biotite (~10 Å). This has not been possible with the conventional transmission pole figure goniometry method. A wide range of texture strengths were observed, with maxima on (001) pole figures ranging from 1.10 m.r.d. in fault gouge to 13.5 m.r.d. in schist (Table 3). We consider all these determinations to be quantitative in the sense that observed diffraction data compare favorably with the calculated Rietveld model (e.g., Fig. 5). In the case of lattice parameters and volume fractions, uncertainties can be described with a standard deviation. For texture patterns, this is not satisfactory because the 3D orientation distribution function (ODF) is highly non-linear and to assign, for example, a standard deviation to a (001) pole figure maximum is not possible. But we can compare observed and calculated diffraction intensities for the (001) peak such as in Fig. 5.

It is appropriate to compare the synchrotron Rietveld method with the conventional X-ray goniometer method. A disadvantage

Table 3
(001) Pole figure minima (top) and maxima (bottom) (in m.r.d.).

	SA #1	SA #2	SA#3	Hornby	Brg 929	Brg 1118	Brg 1295
Illite/mica	0.27	0.51	0.85	0.33			
	1.91	1.79	1.18	3.65			
Illite/smectite	0.48	0.50	0.86	0.35			
	1.97	1.51	1.13	2.35			
Kaolinite				0.27			
				5.59			
Montmorillonite				0.33			
				1.68			
Chlorite					0.10	0.19	0.43
					13.47	6.87	7.10
Biotite							0.11
							10.12
Muscovite					0.19	0.29	0.50
					9.43	8.18	4.52
Graphite						0.11	
						4.54	
Quartz				0.80			
				1.14			

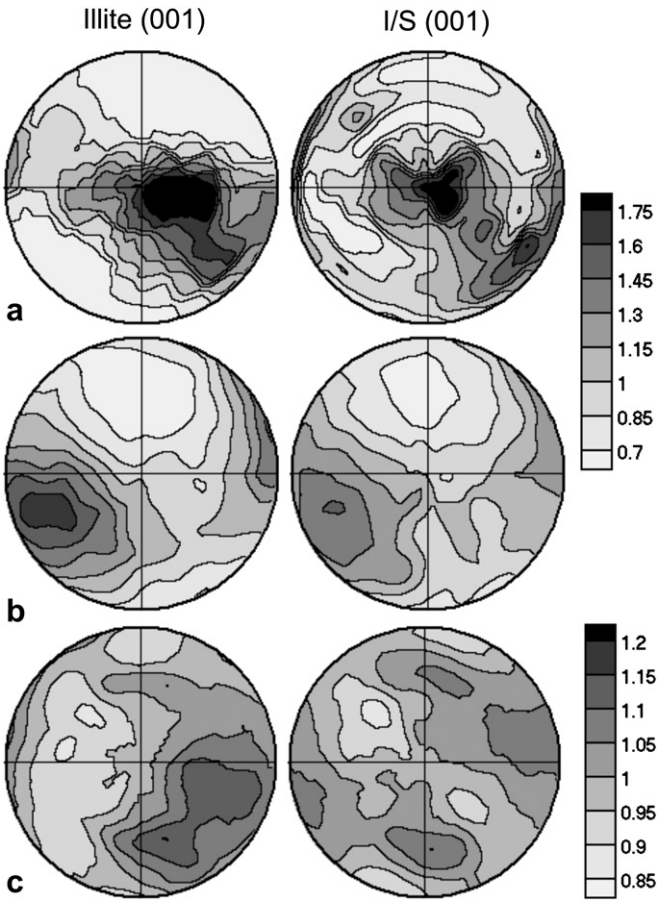

Fig. 6. Pole figures for detrital illite/muscovite/biotite (left) and authigenic illite/smectite in SAFOD fault gouge. (a) #1, (b) #2, (c) #3. Equal area projection, linear contour intervals in multiples of a random distribution. Scale for (c) is different from (a) and (b).

is that users have to write proposals and travel to synchrotron facilities and cannot do measurements in their own laboratories. However, in 2 days of beamtime many samples can be measured and many synchrotrons have beamlines and staff with expertise for experiments such as those described here. Most important though are the real advantages in quantitative characterization. One of the difficult tasks is to obtain a reliable background function in the case of very weak textures and multiple phases, particularly at low diffraction angles where backgrounds increase. This background function as function of Q (i.e., d-spacing, Fig. 4) not only depends on sample tilt but also to a lesser extent on azimuth (Fig. 5). A Rietveld fit of the background function is a better approximation than a simple scan across the diffraction peak in a X-ray goniometer that assumes separated diffraction peaks. Another issue is normalization of the pole figure to express maxima in multiples of a random distribution. In pole figure goniometry, pole figures are incomplete and normalization relies on arbitrary assumptions about the non-measured part. This is particularly significant for estimating pole figure minima which is an important part of texture information. In the seven samples, (001) minima of phyllosilicates range from 0.10 m.r.d. (in schist Brg 929) to 0.86 m.r.d. (in SAFOD #3) (Table 3). Finally, pole figure goniometry of phyllosilicates in rocks has only resolved the orientation of basal planes. With the Rietveld method, we obtain full information about the orientation distribution, including orientation of a-axes.

4.1. Fault gouge

Weak fabrics have been documented for clay minerals in fault gouge (e.g., Chester and Logan, 1987; Haines et al., 2009; Schleicher et al. 2009; White, 2001; Yan et al., 2001). The compilation of Haines et al. describes illite (001) maxima between 2 and 4 m.r.d., though there is no information about pole figure minima. This agrees with our samples, but in addition we can separate detrital and authigenic phyllosilicates, which have obviously different histories. Authigenic illite/smectite are also textured, but the strength is considerably weaker.

In the case of the SAFOD samples, the pole figures are asymmetric and referred to the orientation of the sample slab. The "foliation" was difficult to ascertain and preferred orientation is local and heterogeneous as illustrated by single images (Fig. 7). The sample SAFOD #2 is from a region with pronounced slicken side coating (Fig. 7b). Even here the orientation distribution is weak (001 maximum for illite/mica is 1.79 m.r.d., Fig. 6b). Mineralogic composition of the samples (Solum et al., 2006), including the presence of analcite in SAFOD #3, and talc and serpentine (Moore and Rymer, 2007), as well as amorphous silica (Janssen et al., in press), suggests alteration with dissolution and precipitation at low grade hydrothermal conditions.

Significantly, the orientation distribution of quartz is random. We might have expected that stresses during seismic events may have activated mechanical Dauphiné twinning (Tullis and Tullis, 1972) which initiates around 100 MPa (Wenk et al., 2007) and could have then been used as a piezometer (Hickman and Zoback, 2004).

4.2. Shale

Kimmeridge shale displays an (001) maximum for detrital illite of 3.7 m.r.d. and for kaolinite of 5.6 m.r.d. Minimum pole densities are 0.33 and 0.27 m.r.d., respectively. The texture of authigenic illite/smectite is considerably weaker (2.35 m.r.d. and 0.35 m.r.d.). In addition there is a small amount of poorly oriented montmorillonite (1.59 m.r.d. and 0.41 m.r.d.) established by a weak and broad 14 Å peak. All patterns display axial symmetry about the bedding normal. The a-axes have rotational freedom in the bedding plane.

This is comparable to other studies of shales where (001) pole density maxima range from 2 to 10 (e.g., Aplin et al., 2006; Day-Stirrat et al., 2008; Ho et al., 1999; Kanitpanyacharoen et al., submitted for publication; Lonardelli et al., 2006; Wenk et al., 2008a,b). In those shales, where both illite and kaolinite have been measured, there is considerable variation but kaolinite generally has a stronger texture, as is the case in this Kimmeridge shale. While kaolinite often displays a sharp (001) texture peak superposed on a broad random population, the high random contribution to illite textures (0.33 m.r.d.) is new and more similar to experimentally compressed illite–kaolinite–quartz mixtures (Voltolini et al., 2009).

From preferred orientation patterns of platelet-shaped particles we can use the March (1932) model that relies on rigid particles in a viscous matrix to estimate strain ϵ perpendicular to the bedding. If we allow for volume change during compaction ($\varepsilon = \rho_{max}^{-1/2} - 1$, Oertel and Curtis, 1972) then we get compaction strains for kaolinite of 1.36 and for illite 0.91.

There has been much interest in preferred orientation in shales because of the influence on elastic anisotropy and corresponding directionality of acoustic velocities (e.g., Sayers, 1994). We will analyze the relationship between phyllosilicate textures and elastic anisotropy of the Kimmeridge shale in a separate study (Militzer et al., in press).

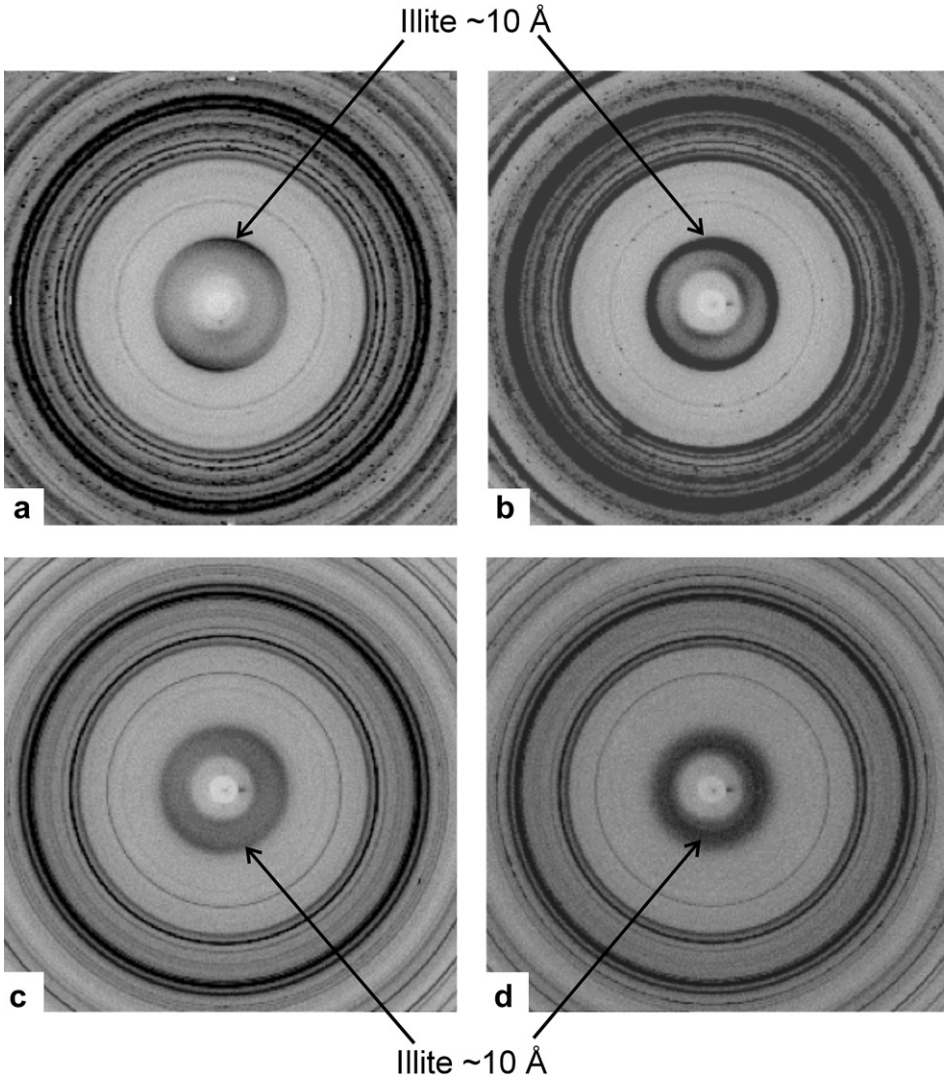

Fig. 7. Selected diffraction images of SAFOD fault gouge. Note particularly the 10 Å diffraction ring (arrow) (a) #1, (b) #2, (c) #3 area A, (d) #3 area B. The strongest texture is displayed in (a), a very weak texture in (c) corresponding to pole figures in Fig. 6c, and a random texture in (d).

4.3. Schist

There is considerable information about phyllosilicate fabrics in slates (e.g., review by Oertel, 1983) but very little about metamorphic schists. The classic review of Sander (1950) establishes the relationship of mica preferred orientation and schistosity but in many metamorphic rocks this is considerably more complex. There are often different generations of phyllosilicates, for example, some coarse porphyroblastic muscovite and fine-grained muscovite associated with feldspar alteration. What is the difference between biotite, muscovite and chlorite fabrics? Here we are not going to come up with general conclusions by analyzing three schists, but rather demonstrate that the hard X-ray method developed for shales (Wenk et al., 2006) is applicable to schists as well.

A main emphasis is on quantifying the orientation of mica *a*-axes. There are a few neutron diffraction studies suggesting increasing alignment with deformation in mylonites (Wenk and Pannetier, 1990; Chateigner et al., 1999); almost random (100) of biotite in gneiss was documented by Helming et al. (1996). A follow-up comparative study by Ullemeyer and Weber (1999) only documents (001) pole figures of biotite in gneisses. Also, an investigation of slaty cleavage development with muscovite and chlorite by pole figure goniometry (Ho et al., 1996) does not address the issue of *a*-axes. Thus this is a wide-open issue.

In this new study, we are particularly interested in the potential alignment of *a*-axes in the lineation direction as suggested by (100) pole figures of Wenk and Pannetier (1990). We are rotating our coordinate system so that we are looking down on the schistosity plane. This gives an undistorted view of the symmetry of the (001) pole figures. It is clear that there is an elliptical distortion in schists (Fig. 9) that is not observed in shale (Fig. 8). It is particularly pronounced in Brg 929 (Fig. 9a), where (100) pole figures show a slight concentration in the lineation direction (Fig. 10a).

In order to determine if the (100) maximum is simply produced by the dispersion of (001) and not a true alignment of *a*-axes, we exported the ODF of triclinic chlorite in Brg 929 from MAUD and calculated corresponding pole figures with BEARTEX (Fig. 11a). Then, we constructed a stochastic ODF by assigning texture weights to 4000 random orientations. In order to make sure that this transformation properly represented the original ODF, we converted the stochastic ODF and recalculated pole figures (Fig. 11b). The two distributions look very similar. The stochastic ODF is slightly weaker because of the cell structure. Of the 3 Euler angles that describe an orientation $\varphi_1\ \Phi\ \varphi_2$ (in Bunge notation), φ_1 and Φ

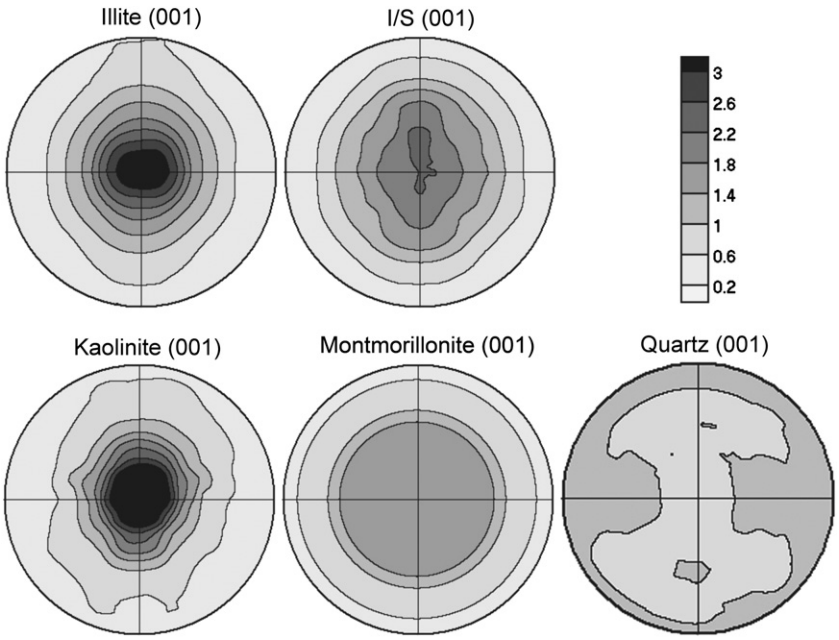

Fig. 8. (001) Pole figures for Kimmeridge shale: illite, illite/smectite, kaolinite, montmorillonite and quartz. Equal area projection, linear contour intervals. Projection is on the bedding plane.

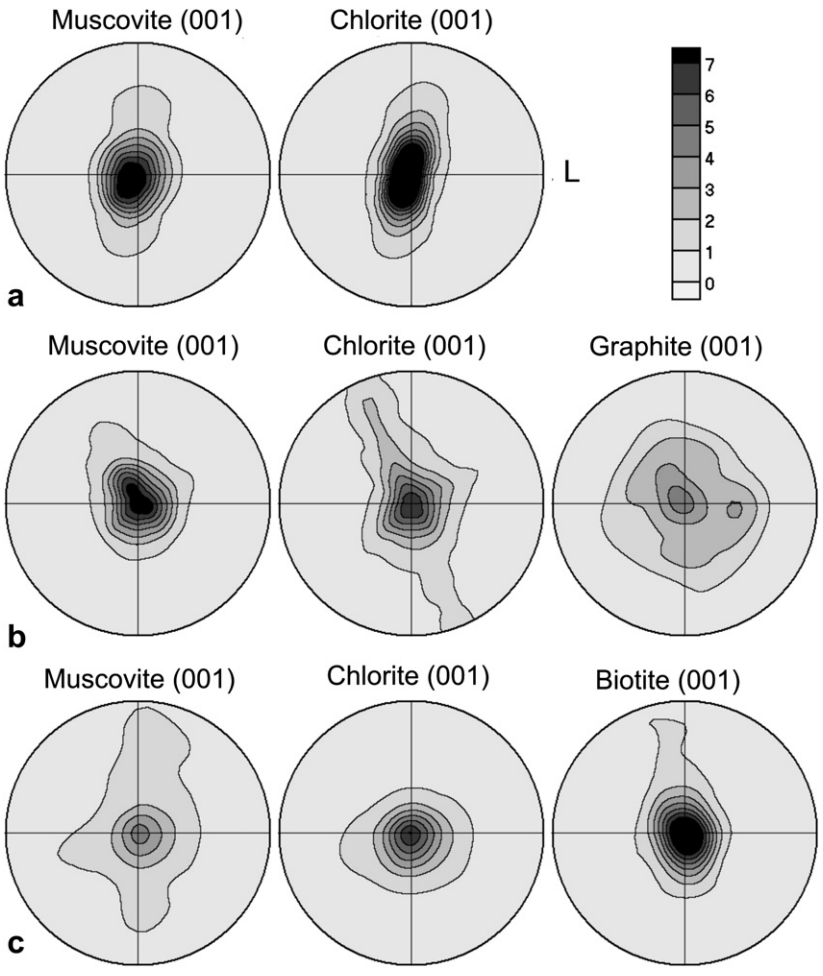

Fig. 9. (001) Pole figures for muscovite, biotite, chlorite and graphite in schists. (a) Brg 929, (b) Brg 1118, (c) Brg 1295. Equal area projection, linear contour intervals. Projection is on the macroscopic foliation and the lineation (*L*) is indicated.

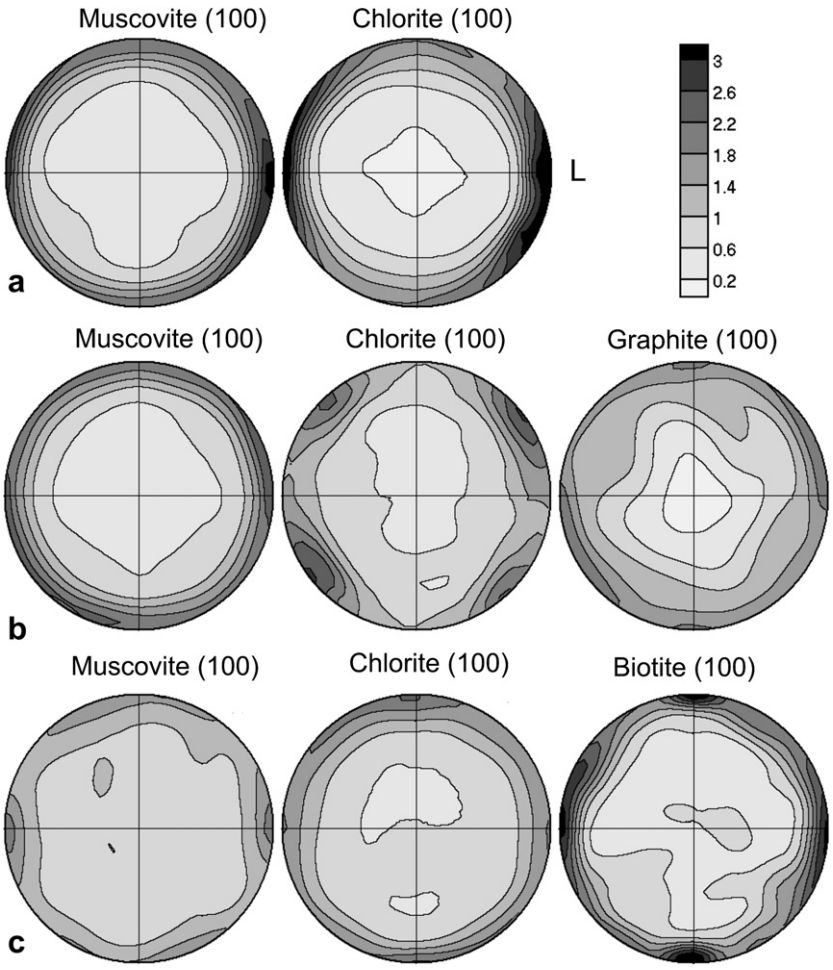

Fig. 10. (100) Pole figures for muscovite, biotite, chlorite and graphite in schists. (a) Brg 929, (b) Brg 1118, (c) Brg 1295. Equal area projection, linear contour intervals. Projection is on the macroscopic foliation and the lineation (L) is indicated.

specify the orientation of the crystal coordinate system z-axis and φ_2 specifies the orientation of the x-axis (around the z-axis). For the convention of assigning a Cartesian coordinate system to a triclinic crystal see, e.g., Matthies and Wenk (2009). Next, we replace for each of the 4000 orientations φ_2 by a random number (between 0° and 360°) and generate additional 12 orientations at $\varphi_2 = 12°$ intervals, thus covering the whole circle around the z-axis. From these 48,000 orientations that do not have a preferential alignment of a-axes, we then generate an OD and calculate corresponding pole figures (Fig. 11c). The (100) and (010) pole figures in Fig. 11b and c are virtually identical, indicating that, at least in this sample, there is no constraint on x-axis alignment, i.e., platelets have rotational freedom. Indeed, looking at the microstructure of Brg 929 (Fig. 2a), we see clear evidence for microfolds and crenulation cleavage. The slight maximum of (100) in the lineation direction for biotite in mylonite (Wenk and Pannetier, 1990) may have a similar cause. A "March-type" orientation for muscovite with rotational freedom of a-axes was suggested for slates (Sintubin, 1998).

Obviously this may not be the case for all phyllosilicate fabrics in schists and should be investigated systematically over a broader range of metamorphic rocks to determine the role of deformation, grain shape anisotropy and dynamic recrystallization on texture development of phyllosilicates in metamorphic rocks. There is evidence to suggest that micas deform by dislocation glide on the basal plane (e.g., Bell and Wilson, 1981; Christofferson and Kronenberg, 1993; Kronenberg et al., 1990; Mares and Kronenberg, 1993; Shea and Kronenberg, 1992, 1993) and dislocations are produced during kinking (Bell et al., 1986), but slip on a single slip plane alone is unlikely to be responsible for the development of preferred orientation. More likely the high shape anisotropy plays an important role by rigid body rotation (Wilson and Bell, 1979). Additionally crystallization and recrystallization under stress are significant (Etheridge and Hobbs, 1974) and thermodynamic theory predicts an alignment of (001) lattice planes perpendicular to the compression direction (e.g., Kamb, 1959; Shimizu, 1997). While there is a strong tendency for alignment of (001) lattice planes, elastic properties (e.g., of muscovite) are close to transverse isotropy ($C_{11} = 181$ GPa, $C_{22} = 178$ GPa, Vaughan and Guggenheim, 1986) and thus unlikely to produce a strong selection for orientation of a-axes.

In greenschist facies Brg 929 the texture of chlorite (13.7 m.r.d.) is stronger than that of muscovite (9.4 m.r.d.). Both minerals are fairly coarse and locally deformed. Greenschist Brg. 1118 is layered with bimodal distributions of muscovite. Coarser muscovite is in layers and very strongly oriented. There is a second type of muscovite in layers of quartz and feldspar porphyroclast (Fig. 2b). In those layers, muscovite is much more random and also these are the layers where most of the chlorite occurs. With our method, which is a volume average, we cannot separate the two types of muscovite but we note a relatively high level of randomly oriented crystallites (0.29 m.r.d.). Chlorite occurs mainly in the quartz-rich

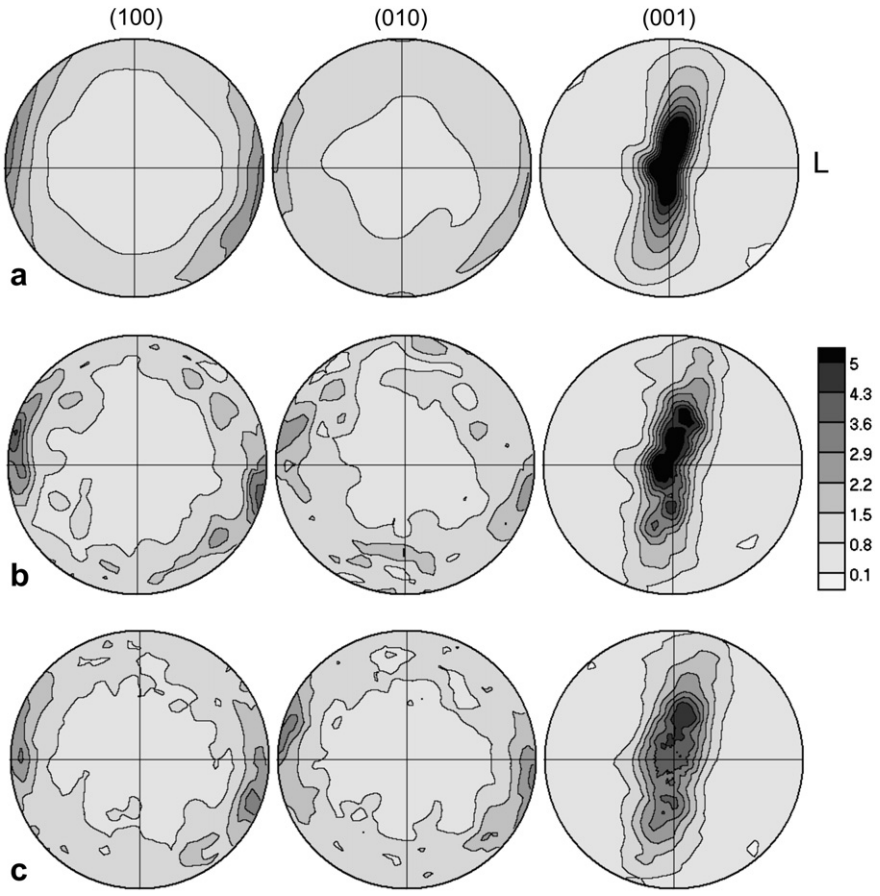

Fig. 11. Modeling pole figures for chlorite of Brg 929. (a) Pole figures recalculated from the MAUD ODF (compare with Fig. 9a but different scale is used). (b) ODF of (a) discretized into 4000 individual orientations and regenerating pole figures. (c) Keeping orientations of *c*-axes but randomizing orientations of *a*-axes and recalculating pole figures. Equal area projection, linear contour intervals.

layers, and thus, its overall texture strength is weaker than muscovite. In the muscovite layers, there are small amounts of very fine-grained graphite with (001) parallel to the schistosity plane. In the higher grade biotite schist (Brg 1295), fairly large biotite and muscovite crystals are strongly aligned (Fig. 2c). But there is a second generation of muscovite and chlorite, replacing older plagioclase, with a much more random texture. Correspondingly, muscovite and chlorite pole figures display weaker textures than biotite pole figures (Fig. 9c) and, as in Brg 1118, with a large percentage of random orientations (0.43 and 0.50 m.r.d. for chlorite and biotite, respectively). In the future, phyllosilicate textures in schists should be examined more systematically. With the method demonstrated here, this is fairly straightforward.

5. Conclusions

A synchrotron hard X-ray method combined with Rietveld refinement has been used to quantify preferred orientation of phyllosilicates in fault gouge, shale and schist. This method has two major advantages over X-ray goniometry: with the Rietveld fit of whole spectra we can deconvolute overlapping peaks, for example, detrital illite/muscovite and authigenic illite/smectite (in all samples investigated so far detrital mica is more strongly oriented than authigenic clay). Secondly, we obtain information about the full crystal orientation, not just the (001) plane, but in all cases investigated so far there appears to be rotational freedom of (001) platelets, including in metamorphic schists. Textures in fault gouge are weak, in shale they are moderate and in schists they are strongest.

Acknowledgements

The project was supported by DOE-BES (DE-FG02-05ER15637) and NSF (EAR-0836402). We acknowledge access to the facilities of beamline 11-ID-C at APS ANL and Y. Ren for assistance with the experiments. Steve Hickman (USGS) got us interested and was giving us the opportunity to analyze SAFOD samples; Brian Hornby (British Petroleum, Houston) provided the classical material of Kimmeridge shale. Luca Lutterotti (Trento) kindly modified the software MAUD to analyze complex materials such as shale. We appreciate thoughtful comments by reviewers, including A. Kronenberg, that helped to improve the manuscript.

References

Aplin, A., Matenaar, I., McCarty, D., van der Pluijm, B., 2006. Influence of mechanical compaction and clay mineral diagenesis on the microfabric and pore-scale properties of deep-water Gulf of Mexico mudstones. Clays and Clay Minerals 54, 500–514.

Bell, I.A., Wilson, C.J.L., 1981. Deformation microstructures of biotite and muscovite: TEM microstructure and deformation model. Tectonophysics 78, 201–228.

Bell, I.A., Wilson, C.J.L., McLaren, A.C., Etheridge, M.A., 1986. Kinks in mica: role of dislocations and (001) cleavage. Tectonophysics 127, 49–65.

Bish, D.L., 1993. Rietveld refinement of the kaolinite structure at 1.5 K. Clays and Clay Minerals 41, 738–744.

Bish, D.L., Von Dreele, R.B., 1989. Rietveld refinement of non-hydrogen atomic positions in kaolinite. Clays and Clay Minerals 37, 289–296.

Chateigner, D., Wenk, H.-R., Pernet, M., 1999. Orientation distributions of low symmetry polyphase materials using neutron diffraction data: application to a rock composed of quartz, biotite and feldspar. Textures and Microstructures 33, 35–43.

Chester, F.M., Logan, J.M., 1987. Composite planar fabric of gouge from the Punchbowl fault, California. Journal of Structural Geology 9, 621–634.

Christofferson, R., Kronenberg, A.K., 1993. Dislocation interactions in experimentally deformed biotite. Journal of Structural Geology 15, 1077–1095.
Collins, D.R., Catlow, C.R.A., 1992. Computer simulation of structures and cohesive properties of micas. American Mineralogist 77, 1172–1181.
Day-Stirrat, R., Aplin, A., Srodon, J., van der Pluijm, B., 2008. Diagenetic reorientation of phyllosilicate minerals in Paleogene mudstones of the Podhale Basin, southern Poland. Clays and Clay Minerals 56, 100–111.
Downs, R.T., Hall-Wallace, M., 2003. The American Mineralogist crystal structure database. American Mineralogist 88, 247–250.
Etheridge, M.A., Hobbs, B.E., 1974. Chemical and deformational controls on recrystallization of mica. Contributions to Mineralogy Petrology 43, 111–124.
Gualtieri, A.F., 2000. Accuracy of XRPD QPA using the combined Rietveld–RIR method. Journal of Applied Crystallography 33, 267–278.
Guggenheim, S., Chang, Y.-H., Koster van Groos, A.F., 1987. Muscovite dehydroxylation: high-temperature studies. American Mineralogist 72, 537–550.
Hammersley, A.P., 1998. Fit2D: V99.129 Reference manual version 3.1. Internal Report ESRF–98–HA01.
Haines, S.H., van der Pluijm, B.A., Ikari, M., Saffer, D., Marone, C., 2009. Clay fabrics in natural and artificial fault gouge. Journal of Geophysical Research 114, B05406. doi:10.1029/2008JB005866.
Helming, K., Schmidt, D., Ullemeyer, K., 1996. Preferred orientations of mica bearing rocks described by texture components. Textures and Microstructures 25, 211–222.
Hickman, S.H., Zoback, M.D., Ellsworth, W.L., 2004. Introduction to special sections: preparing for the San Andreas fault observatory at depth. Geophysical Research Letters 31, L12S01. doi:10.1029/2004GL020688.
Hickman, S., Zoback, M., 2004. Stress orientations and magnitudes in the SAFOD pilot hole. Geophysical Research Letter 31, L15S12. doi:10.1029/2004GL020043.
Ho, N.-C., Peacor, D.R., van der Pluijm, B.A., 1996. Contrasting roles of detrital and authigenic phyllosilicates during slaty cleave development. Journal of Structural Geology 18, 615–623.
Ho, N.-C., Peacor, D.R., van der Pluijm, B.A., 1999. Preferred orientation of phyllosilicates in Gulf Coast mudstones and relation to the smectite–illite transition. Clays and Clay Minerals 47, 495–504.
Hornby, B.E., 1998. Experimental laboratory determination of the dynamic elastic properties of wet, drained shales. Journal of Geophysical Research 103 (B12), 29945–29964.
Janssen, C., Wirth, R., Rybacki, E., Naumann, R., Kemnitz, H., Wenk, H.-R., Dresen, G., Amorphous material in SAFOD core samples (San Andreas Fault): Evidence for crush-origin pseudotachylytes? Geophysical Research Letters 37, in press, doi:10.1029/2009GL04993.
Joswig, W., Fuess, H., Rothbauer, R., Takeuchi, Y., Mason, S.A., 1980. A neutron diffraction study of a one-layer triclinic chlorite (penninite). American Mineralogist 65, 349–352.
Kamb, W.B., 1959. Theory of preferred crystal orientation developed by crystallization under stress. The Journal of Geology 67, 153–170.
Kanitpanyacharoen, W., Wenk, H.-R., Kets, F., Lehr, B.C., submitted for publication. Texture and anisotropy analysis of Qusaiba shales. Geophysical Prospecting.
Knowles, C.R., Rinaldi, R., Smith, J.V., 1965. Refinement of the crystal structure of analcime. Indian Mineralogist 6, 127–140.
Kronenberg, A.K., Kirby, S.H., Pinkston, J., 1990. Basal slip and mechanical anisotropy of biotite. Journal of Geophysical Research 95, 19257–19278.
Lonardelli, I., Wenk, H.R., Lutterotti, L., Goodwin, M., 2005. Texture analysis from synchrotron diffraction images with the Rietveld method: dinosaur tendon and salmon scale. Jouranl of Synchroton Radiation 12, 354–360.
Lonardelli, I., Wenk, H.-R., Ren, Y., 2006. Preferred orientation and elastic anisotropy in shales. Geophysics 72, D33–D40.
Lutterotti, L., Matthies, S., Wenk, H.-R., Schultz, A.J., Richardson, J.W., 1997. Combined texture and structure analysis of deformed limestone from time-of-flight neutron diffraction spectra. Journal of Applied Physics 81, 594–600.
Lutterotti, L., Voltolini, M., Wenk, H.-R., Bandyopadhyay, K., Vanorio, T., 2010. Texture analysis of turbostratically disordered Ca-montmorillonite. American Mineralogist 95, 98–103.
March, A., 1932. Mathematische Theorie der Regelung nach der Korngestalt bei affiner Deformation. Zeitschrift Fuer Kristallographie 81, 285–297.
Mares, V.M., Kronenberg, A.K., 1993. Experimental deformation of muscovite. Journal of Structural Geology 15, 1061–1075.
Matthies, S., Vinel, G.W., 1982. On the reproduction of the orientation distribution function of textured samples from reduced pole figures using the concept of conditional ghost correction. Physica Status Solidi B122, K111–K114.
Matthies, S., Wenk, H.-R., 2009. Transformations for monoclinic crystal symmetry in texture analysis. Journal of Applied Crystallography 42, 564–571.
Militzer, B., Wenk, H.-R., Stackhouse, S., Stixrude, L. First principles calculation of the elastic properties of clay minerals and their application to shale anisotropy. American Mineralogist, in press.
Moore, D.E., Rymer, M.J., 2007. Talc-bearing serpentinite and the creeping section of the San Andreas fault. Nature 448, 795–797.
Oertel, G., 1983. The relationship of strain and preferred orientation of phyllosilicate grains in rocks – review. Tectonophysics 100, 413–447.
Oertel, G., Curtis, C.D., 1972. Clay-ironstone concretion preserving fabrics due to progressive compaction. GSA Bulletin 83, 2597–2606.
Plançon, A., Tsipurski, S.I., Drits, V.A., 1985. Calculation of intensity distribution in the case of oblique texture electron diffraction. Journal of Applied Crystallography 18, 191–196.
Popa, N.C., 1998. The hkl dependence of diffraction-line broadening caused by strain and size for all Laue groups in Rietveld refinement. Journal of Applied Crystallography 31, 176–180.
Redhammer, G.J., Roth, G., 2002. Single-crystal structure refinements and crystal chemistry of synthetic trioctahedral micas $KM_3(Al^{3+}, Si^{4+})_4O_{10}(OH)_2$, where $M = Ni^{2+}$, Mg^{2+}, Co^{2+}, Fe^{2+}, or Al^{3+}. American Mineralogist 87, 1464–1476.
Rule, A.C., Bailey, S.W., 1987. Refinement of the crystal structure of a monoclinic ferroan clinochlore. Clays and Clay Minerals 35, 129–138.
Sander, B., 1930. Gefügekunde der Gesteine. Springer, Berlin.
Sander, B., 1934. Typisierung von deformierten Tonschiefern mit optischen und rontgenoptischen Mitteln. Zeitschrift Fuer Kristallographie 89, 97–124.
Sander, B., 1950. Einführung in die Gefügekunde der Geologischen Koerper, vol. 2. Springer-Verlag, Vienna.
Sayers, C.M., 1994. The elastic anisotropy of shales. Journal of Geophysical Research 99, 767–774.
Schleicher, A., van der Pluijm, B., Solum, J., Warr, L., 2006. Origin and significance of clay-coated fractures in mudrock fragments of the SAFOD borehole (Parkfield, California). Geophysical Research Letter 33. doi:10.1029/2006GL026505.
Schleicher, A.M., Warr, L.N., van der Pluijm, B.A., 2009. On the origin of mixed-layered clay minerals from the San Andreas Fault at 2.5–3 km vertical depth (SAFOD drillhole at Parkfield, California). Contributions to Mineralogy and Petrology 157, 173–178.
Shea, W.T., Kronenberg, A.K., 1992. Rheology and deformation mechanisms of an isotropic mica schist. Journal of Geophysical Research 97, 15201–15237.
Shea, W.T., Kronenberg, A.K., 1993. Strength and anisotropy of foliated rocks with varied mica contents. Journal of Structural Geology 15, 1097–1121.
Shimizu, I., 1997. The non-equilibrium thermodynamics of intracrystalline diffusion under non-hydrostatic stress. Philosophical Magazine A75, 1221–1235.
Sintubin, M., 1998. Mica (110) pole figures in support of Marchian behaviour of phyllosilicates during the development of phyllosilicate preferred orientation. Proceedings of "texture and anisotropy of polycrystals". Materials Science Forum 273–275 p. 601–606.
Solum, J.G., Hickman, S.H., Lockner, D.A., Moore, D.E., van der Pluijm, B.A., Schleicher, A.M., Evans, J.P., 2006. Mineralogical characterization of protolith and fault rocks from the SAFOD main hole. Geophysical Research Letters 33, L21314. doi:10.1029/2006GL027285.
Tsipursky, S.I., Drits, V.A., 1984. The distribution of octahedral cations in the 2:1 layers of dioctahedral smectites studied by oblique-texture electron diffraction. Clay Minerals 19, 177–193.
Tullis, J., Tullis, T.E., 1972. Preferred orientation produced by mechanical Dauphiné twinning. Thermodynamics and axial experiments. American Geophysical Union Monograph 16, 67–82.
Ullemeyer, K., Weber, K., 1999. Lattice preferred orientation as an indicator of a complex deformation history of rocks. Textures and Microstructures 33, 45–60.
Van der Pluijm, B.A., Ho, N.-C., Peacor, D.R., 1994. High-resolution X-ray texture goniometry. Journal of Structural Geology 16, 1029–1032.
Vaughan, M.T., Guggenheim, S., 1986. Elasticity of muscovite and its relationship to crystal structure. Journal of Geophysical Research 91, 4657–4664.
Voltolini, M., Wenk, H.-R., Mondol, N.H., Bjørlykke, K., Jahren, J., 2009. Anisotropy of experimentally compressed kaolinite–illite–quartz mixtures. Geophysics 74, D13–D23.
Wenk, H.-R., Pannetier, J., 1990. Texture development in deformed granodiorites from the Santa Rosa mylonite zone, southern California. Journal of Structural Geology 12, 177–184.
Wenk, H.-R., Matthies, S., Donovan, J., Chateigner, D., 1998. BEARTEX, a Windows-based program system for quantitative texture analysis. Journal of Applied Crystallography 31, 262–269.
Wenk, H.-R., Lonardelli, I., Franz, H., Nihei, K., Nakagawa, S., 2006. Texture analysis and elastic anisotropy of illite clay. Geophysics 72, E69–75.
Wenk, H.-R., Bortolotti, M., Barton, N., Oliver, E., Brown, D., 2007. Dauphiné twinning and texture memory in polycrystalline quartz. Part 2: in situ neutron diffraction compression experiments. Physics and Chemistry of Minerals 34, 599–607.
Wenk, H.-R., Voltolini, M., Mazurek, M., Van Loon, L.R., Vinsot, A., 2008a. Preferred orientations and anisotropy in shales: Callovo-Oxfordian shale (France) and Opalinus Clay (Switzerland). Clays and Clay Minerals 56, 285–306.
Wenk, H.-R., Voltolini, M., Kern, H., Popp, H., Mazurek, M., 2008b. Anisotropy of Mont Terri Opalinus Clay. The Leading Edge 27, 742–748.
White, S.R., 2001. Textural and microstructural evidence for semi-brittle flow in natural fault rocks with varied mica contents. International Journal of Earth Sciences (Geologische Rundschau) 90, 14–27.
Wilson, C.J.L., Bell, I.A., 1979. Deformation of biotite and muscovite: optical microstructures. Tectonophysics 58, 179–200.
Yan, Y., van der Pluijm, B.A., Peacor, D.R., 2001. Deformation microfabrics of clay gouge, Lewis Thrust, Canada: a case for fault weakening from clay transformation. In: Geological Society, Special Publication, 186 103–112.